

# In-ice Radio Signatures of Cosmic Ray Particle Cascades

Simon Chiche<sup>a</sup>, Simona Toscano<sup>a</sup>, Krijn D. de Vries<sup>b</sup>

<sup>a</sup>*Inter-University Institute For High Energies (IIHE), Université libre de Bruxelles (ULB), Boulevard du Triomphe 2, 1050 Brussels, Belgium*

<sup>b</sup>*Vrije Universiteit Brussel, Physics Department, Pleinlaan 2, 1050 Brussels, Belgium*

---

## Abstract

To detect ultra-high-energy neutrinos, experiments such as the Askaryan Radio Array and the Radio Neutrino Observatory in Greenland target the radio emission induced by these particles as they cascade in the ice, using deep in-ice antennas at the South Pole or in Greenland. A crucial step toward this goal is the characterization of the in-ice radio emission from cosmic-ray-induced particle showers. These showers form a primary background for neutrino searches, but can also be used to validate the detection principle and provide calibration signals for in-ice radio detectors. In this work, we use the Monte-Carlo framework FAERIE to perform the first characterization of cosmic ray signals with simulations that incorporate both their in-air and in-ice emissions. We investigate cosmic ray signatures such as their radiation energy, timing, polarization and frequency spectrum and quantify how they depend on shower properties. These results provide key guidelines for cosmic-ray identification and cosmic-ray/neutrino discrimination in future in-ice radio experiments.

*Keywords:* Radio-detection, In-ice experiments, High-energy astroparticles, Monte-Carlo simulations

---

## 1. Introduction

Ultra-high energy neutrinos ( $E > 10^{16}$  eV) are unique messengers for probing the high energy Universe. These particles travel with no deflection nor attenuation and serve as an unambiguous probe of hadronic acceleration [1]. The first detection of an ultra-high neutrino by KM3NeT in 2023 [2] has provided a proof of their existence, further motivating the need for their detection. Yet, neutrino detection is challenging and requires to build experiments with unprecedented field of view, sensitivity, and angular resolution to address the low fluxes at the highest energies and open a new astronomical window [3]. In-ice radio detection of astroparticles is a particularly promising technique. When a neutrino crosses the ice, it induces a cascade of secondary particles that emit radio waves through the Askaryan mechanism [4, 5, 6], coherent at around hundreds of MHz. These radio waves can then be detected with radio antennas buried deep inside the ice sheet. The attenuation length of radio waves in polar ice being typically ten times larger than the one for optical light [7], which makes radio detection a suitable technique to instrument large effective volumes at relatively low costs [8]. Cur-

rent experiments such as the Askaryan Radio Array [9] (ARA) and next-generation detectors including the Radio Neutrino Observatory in Greenland [10] (RNO-G), the Radar Echo Telescope [11] (RET) and IceCube-Gen2 radio [12, 13], therefore aim to deploy radio antennas at the South Pole or in Greenland to detect ultra-high energy neutrinos. Such a detection is not trivial as it requires to identify neutrinos solely from their radio signatures. Cosmic rays in particular are a major background since they can produce radio waves that resembles the neutrino emission and that can also reach the deep antennas. The cosmic ray flux is expected to be at least 1000 times larger than the neutrino flux which implies that cosmic ray/neutrino discrimination is essential to detect ultra-high energy neutrinos. On the other hand, cosmic ray detection would provide a unique opportunity to validate the detection principle of in-ice experiments, as recently reported by the ARA collaboration [14], and help calibrate the detectors. FAERIE [15] is a numerical tool that combines both CORSIKA [16] and GEANT4 [17] Monte-Carlo codes, coupled with the CoREAS radio extension [18], to allow us to simulate the radio emission from cosmic ray particle cascades, as seen by deep in-ice observers. In this work, we use FAERIE to perform an exhaustive characterization of

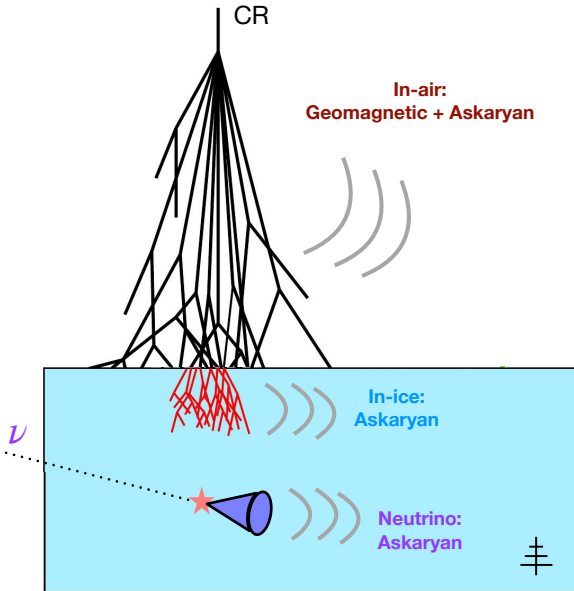


Figure 1: Sketch of a cosmic ray particle cascade and associated emissions. A first emission comes from the in-air cascade (black lines). This emission propagates in the atmosphere and is transmitted to the ice. Another emission is generated directly by the in-ice cascade (red lines) and can also reach deep in-ice antennas. For comparison a typical neutrino event is also shown.

cosmic ray radio emission. We investigate the physical properties of the radio emission, such as the radiation energy, the frequency spectrum, the polarization and the timing and evidence signatures for cosmic ray identification and cosmic ray/neutrino discrimination with in-ice radio detectors.

## 2. General characteristics of the emission

### 2.1. Emission principle

We illustrate the principles of cosmic ray radio emission in Fig. 1. When a cosmic ray enters the atmosphere, it induces an air shower, i.e., a cascade of secondary particles [19]. This cascade emits radio waves [20] that can propagate from the air to the ice and reach deep in-ice antennas, as indicated by the red “in-air” emission on the sketch. Additionally, if the shower is energetic enough, some particles from the air shower can also penetrate the ice and trigger an in-ice particle cascade. This secondary cascade will also emit radio waves, as indicated by the blue “in-ice” emission on the sketch.

The radio emission from the in-air cascade is typical of an air shower and is the result of two main mechanisms: the geomagnetic and the Askaryan emissions [21, 20]. The geomagnetic emission is the dominant mechanism. It originates from the deflection of the lightest charged particles in the shower, namely electrons and positrons, by the Earth’s magnetic field. This deflection creates a transverse current orthogonal to the shower propagation axis. The time variation of this current results in radio emission linearly polarized in the  $\mathbf{v} \times \mathbf{B}$  direction, where  $\mathbf{v}$  is the direction of propagation of the shower and  $\mathbf{B}$  corresponds to the local direction of the Earth’s magnetic field. The Askaryan emission is subdominant in air, it comes from the ionization of the propagation medium by high energy shower particles which creates a net negative charge building up at the shower axis. The time variation of this negative charge yields a radio emission radially polarized in a plane perpendicular to the shower propagation axis.

For the radio emission from the in-ice cascade, the Askaryan mechanism is the only contribution, as the geomagnetic mechanism is suppressed in dense media. The amplitude of the in-ice Askaryan emission is therefore expected to be significantly higher than that of the in-air Askaryan component, since this emission scales with the density of the medium in which the shower develops. Likewise, neutrino primaries interact directly in the ice and produce radio emission solely through the Askaryan mechanism. As a result, the in-ice radio emission from cosmic-ray showers can closely resemble that induced by neutrinos.

In both air and ice emissions, the radio signal is emitted predominantly within a cone around the shower axis, with a maximum intensity at the so-called Cherenkov angle, as illustrated by the purple conical region in Fig. 1. This Cherenkov compression arises from the relativistic propagation of the shower particles, which causes the radiation emitted from different points along the shower axis to arrive in phase at the Cherenkov angle [22, 23]. As a result, the radio signal on the Cherenkov cone is highly coherent, extending to higher frequencies and exhibiting a rapid spatial variability.

### 2.2. FAERIE simulations

While commonly used Monte-Carlo codes such as ZHAireS [24] and CoREAS [18] can simulate the in-air component of cosmic ray radio emission and propagate it down to the Earth’s surface, these tools cannot currently propagate the emission below the ice nor generate the in-ice component, as the rapid variation of the ice density with depth bends the emission and requires to implement ray tracing. On the other hand, FAERIE [15]

is a recently developed numerical tool, that combines the CoREAS and GEANT4 Monte-Carlo codes, coupled to the endpoint formalism [25] and a ray tracing algorithm, to simulate both the in-air and the in-ice radio emission from cosmic ray particle cascades, as seen by deep in-ice observers [26, 27]. In this work, we use the FAERIE framework to investigate in-ice radio signatures of cosmic ray particle showers and perform the first characterization of their emission in a dense inhomogeneous medium.

Running a given FAERIE simulation requires to give as inputs the primary particle nature (mass composition), energy and arrival direction (zenith and azimuth angle). The user must also specify a list of antenna positions that can be above or below the Earth's surface (i.e., the air/ice boundary) at which the emission is evaluated. The outputs are the three components electric field time traces at each antenna for both the in-air component ( $E_x^{\text{air}}(t)$ ,  $E_y^{\text{air}}(t)$ ,  $E_z^{\text{air}}(t)$ ) and the in-ice component ( $E_x^{\text{ice}}(t)$ ,  $E_y^{\text{ice}}(t)$ ,  $E_z^{\text{ice}}(t)$ ) stored independently. The outputs are given in the CoREAS reference frame, with  $x$ : North-South,  $y$ : West-East, and  $z$ : Up-Down. In Fig. 2 we illustrate outputs of FAERIE simulations for the in-air (left-hand panel) and in-ice (right-hand panel) components by showing the East-West channel of the electric field time traces for antennas located at a depth of 100 meters below the ice and at various radial distances from the shower core. The typical cosmic ray radio emission corresponds to a sharp pulse with an a width of a few nanoseconds and an amplitude of a few to thousands of  $\mu\text{V}/\text{m}$ . The figure also shows that the signal varies with the antenna positions depending on their distance to the Cherenkov cone which is found for this specific shower at  $r_{\text{cer}}^{\text{air}} \sim 45 \text{ m}$  and  $r_{\text{cer}}^{\text{ice}} \sim 145 \text{ m}$  for the in-air and in-ice components respectively.

### 2.3. Simulation setup

Using FAERIE, we simulated the radio emission of cosmic ray showers with different primary energy and arrival directions, to build a library of events and perform the first characterization of their emission as seen by deep in-ice observers. FAERIE is a computationally expensive tool, with a single simulation that can run for  $\sim 10^4 - 10^5$  CPU hours, which corresponds to approximately 3 weeks of calculation when run in parallel on the T2B condor cluster. As a consequence, to build our library of events we ran only one shower per set of primary particle energy and zenith angle. While this does not allow us to fully characterize effects related to shower-to-shower fluctuations, this still allows

us to capture the main global characteristics of cosmic ray radio emission and their dependencies with the shower parameters. Furthermore we mitigated our results by running 10 identical showers with a primary energy  $E = 10^{16.5} \text{ eV}$  and zenith angle  $\theta = 0^\circ$  to estimate the uncertainties in our results related to shower-to-shower fluctuations.

#### 2.3.1. Shower input parameters

For our library, we simulated, using QGSJETII-04 as hadronic model, 24 proton simulations with parameters given in Table 1. We considered three primary particle energies generated in logarithmic scale in the range  $[10^{16.5} - 10^{17.5}] \text{ eV}$ . This range was chosen as showers with energies equal or below  $E = 10^{16} \text{ eV}$  will hardly trigger the detector and as the statistics of showers with energies equal or above  $E = 10^{18} \text{ eV}$  is too low to contribute significantly to cosmic ray detections. Though at ultra-high energy the cosmic ray composition is expected to be mainly heavy [28], we simulated only proton primaries as their larger shower-to-shower fluctuations should provide us with results that encompass the typical signals expected for heavier primaries such as iron. This choice was also motivated by the fact that a few test iron simulations run with FAERIE does not show significant differences with analog proton simulations. At first order, cosmic ray radio emission should scale with the cosine of the shower zenith angle, hence zenith angles were generated uniformly in  $\cos \theta$  between  $\theta = 0^\circ$  and  $\theta = 50^\circ$ . We did not simulate more inclined showers since (1) no in-ice component of cosmic ray emission is expected for very inclined showers (see Section 10) and (2) FAERIE currently relies on a flat-Earth description, an assumption that breaks when considering very inclined showers which can propagate in the atmosphere for hundreds of kilometers. The simulation library was designed for a typical Greenland in-ice detector such as RNO-G, hence the magnetic field was set to the one of Summit Station where RNO-G is located, with amplitude  $B_x = 7.7 \mu\text{T}$ ,  $B_z = -54.1 \mu\text{T}$ . This magnetic field being near-vertical, we considered only one azimuth angle for our library of events ( $\varphi = 0^\circ$ , shower propagating towards the magnetic North) as we do not expect significant variations of the radio emis-

<b>Energy [eV]</b>	$10^{16.5}; 10^{17}; 10^{17.5}$
<b>Zenith [°]</b>	0; 20; 28; 34; 39; 43; 47; 50
<b>Depth [m]</b>	0; 40; 60; 80; 100

Table 1: Primary energy, zenith bins and depths of the FAERIE simulation set.

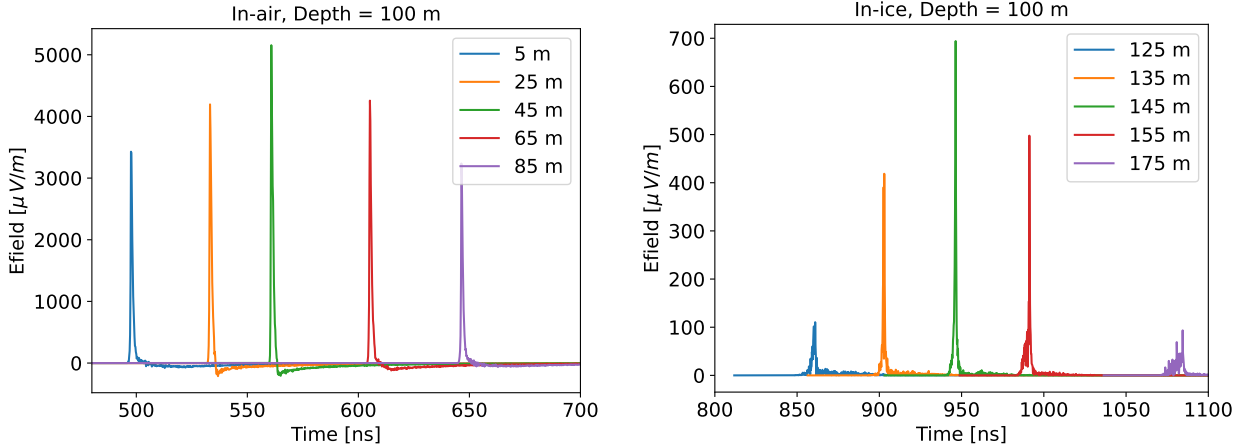


Figure 2: East-West component of the electric field simulated with FAERIE for the in-air (*left*) and in-ice (*right*) component of cosmic ray radio emission for a proton-induced shower with primary energy  $E = 10^{17.5}$  eV and zenith angle  $\theta = 34^\circ$ . Antennas are located at a depth of 100 m and placed at various radial distances from the shower core.

sion with the shower azimuth angle. We further note that Greenland magnetic field has a similar amplitude and direction to the magnetic field at the South Pole, a location which can also host in-ice radio detectors. The main difference between both magnetic field fields being the polarity of the  $z$ -component (downwards in Greenland and upwards in South Pole). Hence our simulations could also be partly relevant for South Pole experiments such as the planned IceCube-Gen2 radio detector. All our simulations were run with a relative thinning of  $10^{-4}$ , a value chosen to mitigate the precision of the simulations with the time computation. All the results shown in study are filtered in the 50 – 1000 MHz band to match the realistic range of observed signals.

### 2.3.2. Ice refractive model

To run a FAERIE simulation we must also specify the ice density model. We used an exponential ice model based on measurements of the ice properties in Greenland, following [29]:

$$n(z) = A - B \exp -C|z|, \quad (1)$$

where  $n$  is the ice refractive index,  $|z|$  is the depth of the antennas and  $A$ ,  $B$ ,  $C$  are parameters of the model. Greenland ice has a discontinuity around a depth of  $|z| = 14.9$  m due to a change in the ice compactification. Hence the refractive index is best fitted using a double exponential model, i.e., two sets of parameters depending on the depth. Following [29] we used,  $A = 1.775$ ,  $B = 0.5019$ ,  $C = 0.03247$  for  $|z| < 14.9$  m and  $A = 1.775$ ,  $B = 0.448023$ ,  $C = 0.02469$  for  $|z| > 14.9$  m.

### 2.3.3. Antenna grid

We considered a 3D grid of 4704 antennas corresponding to three layers of 1568 positions each, located at a depth of 0 m (surface), 60 meters and 100 meters, as illustrated in the left-hand panel of Fig. 3. These depths were chosen to match those of the RNO-G detector. For the same reason, the air-ice boundary is set at an altitude of 3216 meters, corresponding to the one of Summit Station in Greenland. A typical antenna layer is shown in the right-hand panel of Fig. 3. We used a polar grid of antennas with a dense circular core between 0 and 250 meters from the shower impact point, and 24 outer arms, evenly spaced of  $15^\circ$  each, for larger radial distances. The spacing of the inner core is fixed for every simulations, while the spacing of the outer arms is logarithmic and increases with the depth of the antenna layer and the shower zenith angle, to account for the fact that the footprint size increases with the distance to emission source. This specific grid was designed to capture both the specificities of the radio emission from the in-ice component, which requires a dense grid independently of the shower parameters, and those of the in-air component, which requires a sparse zenith-dependent spacing (see discussion Section 2.6). Furthermore, as also shown in Fig. 3, we shifted antenna layers below the surface so that our grid is always centered on the radio emission footprints. The offset was calculated by propagating a ray along the shower axis below the surface using Snell-Descartes's law.

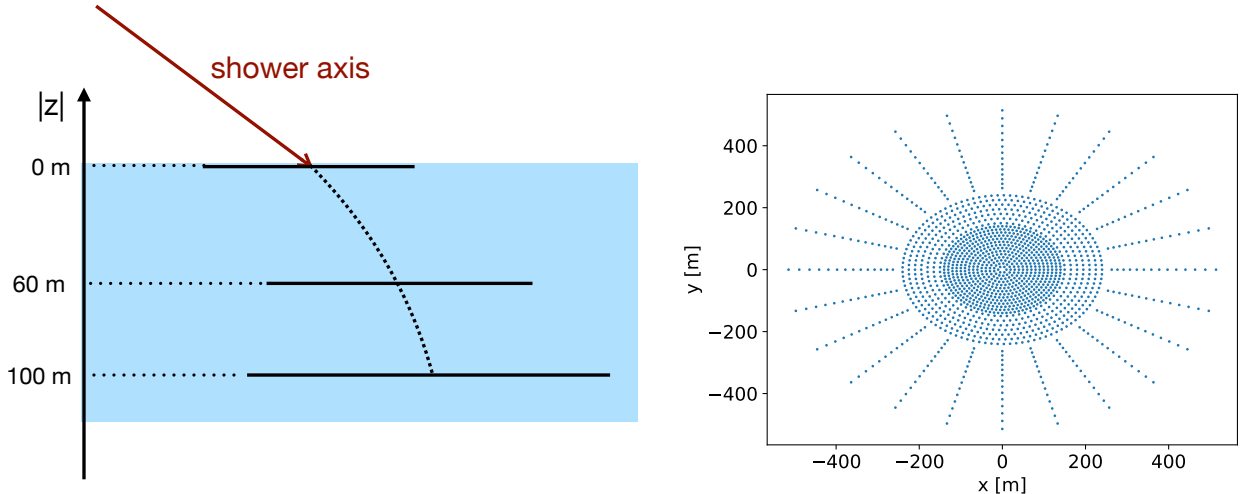


Figure 3: (Left) Sketch of antenna layers at various depths below the ice surface. The red arrow represents the shower axis, the black dotted curved line shows the in-ice continuation of the shower axis using Snell-Descartes law. Each antenna layer is centered on its intersection with the dotted line. The layer width increases with depth. (Right) Typical antenna layout for a given layer. The central region is a dense core with 10-m spacing out to 150 m, followed by 15-m spacing up to 250 m. Beyond this, the array extends into 24 radial arms separated by  $15^\circ$ , with antennas placed along each arm at logarithmically increasing radial distances. Each given layer has 1568 antennas, the full grid corresponds to 4704 simulated antennas.

#### 2.4. Distribution of shower maximum

We characterized our simulation library by evaluating the shower maximum  $X_{\max}$  of the in-air and the in-ice cascades. The left-hand panel in Fig. 4, shows the height above sea level of the in-air  $X_{\max}$  as a function of the shower zenith angle. As expected, inclined showers have their  $X_{\max}$  at higher altitude than vertical ones since the inclined showers propagate longer in the upper atmosphere. We further note that at fixed zenith angle, more energetic showers usually have a deeper  $X_{\max}$  height, since the  $X_{\max}$  grammage scales logarithmically with the primary energy [30, 31]. Eventually, we observe that for vertical showers, with a zenith angle  $\theta = 0^\circ$ ,  $X_{\max}$  can even be below the ice surface. This implies that in such cases the in-air cascade is not yet fully developed when it reaches the ground, leading to clipping effects [32]. Hence, in all the further results that we will show the case of vertical showers should therefore be treated with care and analyzed separately because of this effect. In Fig. 5, we show the  $X_{\max}$  grammage of our simulations. Though the  $X_{\max}$  should not depend on the shower zenith angle, we can observe variations of the grammage even at fixed primary energy which are related to shower-to-shower fluctuations. Still, we get a mean  $X_{\max}$  grammage of  $\sim 670 \text{ g/cm}^2$  at  $10^{16.5} \text{ eV}$  and of  $\sim 740 \text{ g/cm}^2$  at  $10^{17.5} \text{ eV}$ , which are typically expected values with QGSJETII-04.

In the right-hand panel of Fig. 4, we show the slant

depth of the in-ice  $X_{\max}$ , i.e., the distance of the in-ice  $X_{\max}$  from the shower core. Here, we observe that all simulated showers have their in-ice  $X_{\max}$  at around the same distance from the shower core, independently of the primary particle energy or zenith angle. This is a striking feature as it points towards universality of the in-ice cores induced by cosmic ray particle cascades.

#### 2.5. Radio emission footprints

Using FAERIE, we evaluated the radio footprints of our simulations as a function of the antenna depths and the shower parameters. For this, we derived the energy fluence of the radio emission at each antenna, which measures the energy per unit of surface and is given by integrating over time the squared electric field following [32]

$$f_{x,y,z}(x, y) = \epsilon_0 c \int_0^t E_{x,y,z}^2(t, x, y) dt, \quad (2)$$

where  $\epsilon_0$  is the vacuum permittivity and  $c$  is the speed of light in vacuum. The total energy fluence at each antenna is then derived from the sum of its three components  $f_{\text{tot}} = f_x + f_y + f_z$ . In Fig. 16, we show interpolated footprints of the total energy fluence from the in-air and in-ice component for a vertical proton shower with zenith angle  $\theta = 0^\circ$  [lines (a) and (b) respectively]

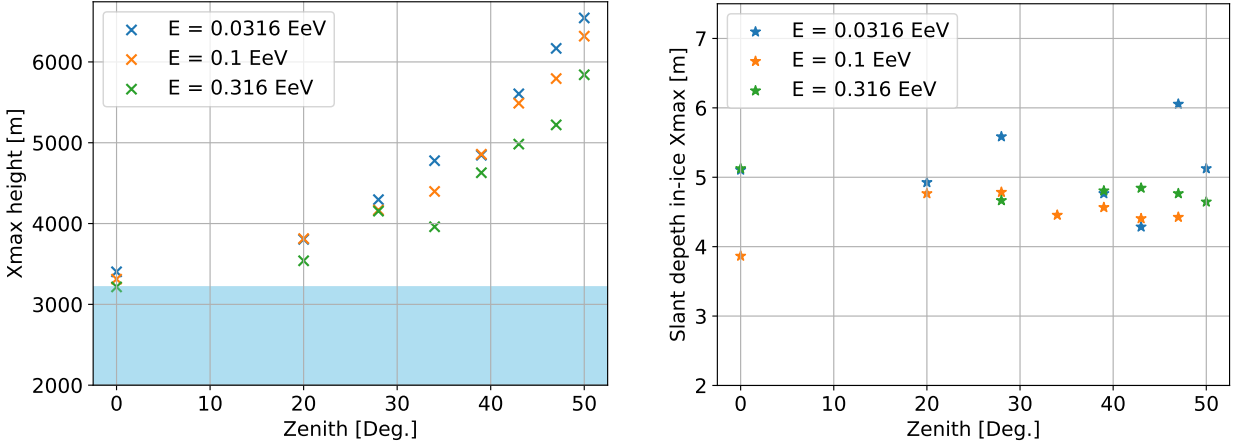


Figure 4: (Left) Height above sea level of the in-air shower maximum  $X_{\max}$  from FAERIE simulations, as a function of the shower zenith angle, for different primary energies (colors). The blue shaded area indicates the ice surface. (Right) Slant depth (along the shower axis), of the in-ice shower maximum, as a function of the shower zenith angle, for the same simulation set.

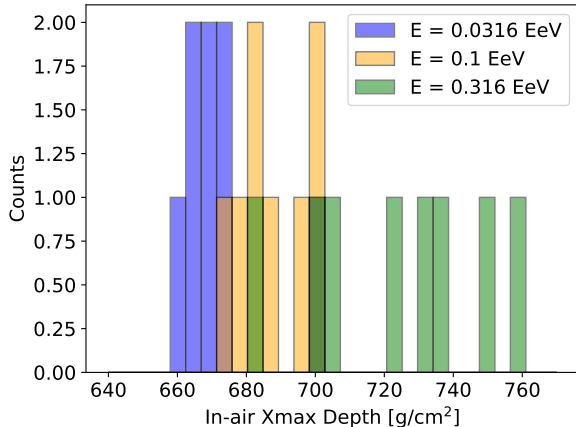


Figure 5: Distributions of the in-air shower maximum grammage  $X_{\max}$ , for different primary energies.

and for a shower with  $\theta = 50^\circ$  (lines (c) and (d)] and primary energy  $E = 10^{17.5} \text{ eV}$ . The results are shown for the three different depths, 0, 60, and 100 meters from left to right. The results are shown here for only one primary energy, but we note that lower primary energies overall yield similar results with lower energy fluence at the antennas.

Looking first at the in-air emission from the vertical shower [line (a)], it can be seen that the radio footprint follows a bean-shaped pattern with a stronger emission on the negative  $y$ -axis and a weaker emission on the positive  $y$ -axis. This feature is well-known and expected from the interferences between the geomagnetic and charge-excess mechanisms. Indeed, as detailed in Sec-

tion 2.1, the geomagnetic emission is linearly polarized toward the  $-\mathbf{v} \times \mathbf{B}$  direction while the charge-excess has a radial polarization. This implies that on one side of the  $\mathbf{v} \times \mathbf{B}$  axis positive interferences between both mechanisms are expected, while on the other side destructive interferences are expected, leading to this bean-shaped pattern. We also notice that no clear Cherenkov features is visible for the in-air emission which is expected when the Cherenkov angle is small and the observer is close from  $X_{\max}$ . This is typically the case for showers in Greenland due to the high altitude above sea level which yields an in-air  $X_{\max}$  very close to the ground, as shown in Fig. 4. In line (b) we show the in-ice emission of the same shower. The maps at a depth of 60 and 100 meters show a clear rotationally symmetric high amplitude Cherenkov ring structure. We also note that while the in-ice emission should be focused in a cone around the shower axis, the map of surface antennas (depth = 0 m) shows a non-negligible emission very close to the shower core ( $x = 0, y = 0$ ). This feature was not reported before but can be expected as the in-ice cascade develops very close to the ice surface. Yet, its amplitude is usually too weak to be detected.

When the showers are inclined, both the in-air and the in-ice emissions are modified, as shown by lines (c) and (d). A first notable change for both emissions is that for inclined showers, the radio footprints of deep antenna layers are no longer centered on the shower core ( $x = 0, y = 0$ ) but shifted towards the shower propagation direction, corresponding to the positive  $x$ -axis here. For the in-air emission [line (c)], we also note that the footprints are elongated towards the shower propagation direction,

which is only a geometrical effect linked to the position of the in-air shower maximum with respect to the ice surface. For the in-ice emission [line (d)], we notice that the radio footprint is no longer rotationally symmetric but deformed. This deformation increases with depth and is linked to the bending of the radio emission as it propagates in the ice, due to the varying refractive index of the medium.

Comparing the amplitude of the different footprints, we observe that for the vertical shower the maximal amplitude of the in-ice emission is higher than that of the in-air emission, while for the inclined shower the in-ice emission amplitude gets very weak and much lower than the one of the in-air footprint, a feature that will be further discussed in Section 10. Looking at the evolution of the footprint amplitude with depth, we also notice that when going to deeper layers, the amplitude of the in-ice emission decreases rapidly, by a factor 2 to 3. On the other hand, the amplitude of the in-air emission decreases but much less significantly with almost no variation between a depth of  $|z| = 60$  meters and  $|z| = 100$  meters for the inclined shower. This effect is purely geometrical. The in-ice  $X_{\max}$  is closer to the observer than the in-air  $X_{\max}$ , so the relative distance to the emission source varies more rapidly with depth for the in-ice component. We also mention that the amplitude variation with depth for the in-air component is expected to decrease with increasing shower zenith angle, as the shower maximum gets further away from the observer (Fig. 4). This is a striking feature as it means that the rapid variation of the amplitude of the in-ice signal with depth could be used to remove any background source that emits radio waves far from the surface, such as airplanes [33], and identify cosmic ray or neutrino signals.

Finally, we mention that for the in-ice emission of the vertical shower observed at a depth of 100 meters [right-hand panel in line (d)] the footprint shows a low-amplitude double ring structure. This feature is seen consistently in our simulations when the energy of the in-ice cascade is high enough. Although the origin of this feature is still under investigation, it seems to be related to an interference pattern seen in the frequency domain (see discussion in Section 4.1). If confirmed, this feature could be a distinctive feature of in-ice cosmic ray radio emission that could be used for their identification. Yet, the amplitude of this component being very low, it might only be detectable for very energetic particle cascades.

## 2.6. Lateral distribution functions

To characterize the evolution of the radio footprint spatial dependency with the shower parameters, we also evaluated the lateral distribution function (LDF) of the emission, which corresponds to the electric field peak amplitude along a given baseline of antennas. In Fig. 6 we show the LDF of the in-air (left-hand panels) and the in-ice (right-hand panels) emissions, along the  $x$  (North-South) axis, at a depth of 60 (top panels) and 100 (bottom panels) plots, for cosmic ray showers with a primary energy  $E = 10^{17.5}$  eV and various zenith angles.

As mentioned in the previous section, it is striking on these plots that the variation of the signal amplitude with depth is more important for the in-ice component than for the in-air one. These plots also highlight the minor Cherenkov feature for the in-air emission and the distinctive two peaks for the in-ice component. We also notice that when increasing the zenith angle, the in-ice emission amplitude decreases and becomes asymmetric. Interestingly the small peak related to the second ring observed in Fig. 16 seems to be always at the same position around  $\pm 190$  m, even when the shower gets more inclined. Eventually we point that independently of the shower zenith angle the in-ice radio emission footprint does not extend over more than  $\pm 200$  m, which justifies the choice of the dense core in our antenna grid in Fig. 3.

For the in-air emission, two effects are in competition when the shower gets inclined. First, the shower maximum  $X_{\max}$ , i.e., the point-source-like of the emission becomes further away from the antenna grid which implies that the LDF extends over larger distances but also that the radio emission amplitude decreases accordingly by energy conservation. On the other hand, inclined showers have their in-air  $X_{\max}$  higher in the atmosphere (Fig. 4), leading to a stronger transverse current due to the lower density in which the shower develops and a higher radiated energy from the geomagnetic mechanism [32](see also Section 2.5). This explains why intermediate zenith angles tend to have the LDF with the highest maximal amplitude, as seen here for  $\theta = 39^\circ$ .

## 3. Radiation energy

In order to constrain global characteristics of cosmic ray radio signals we evaluated the radiation energy of the emission. The radiation energy is obtained by integrating the energy fluence over a given antenna layer, following [32]:

$$E_{\text{rad}} = \int_{x_{\min}}^{x_{\max}} \int_{y_{\min}}^{y_{\max}} f(x, y) \, dx \, dy. \quad (3)$$

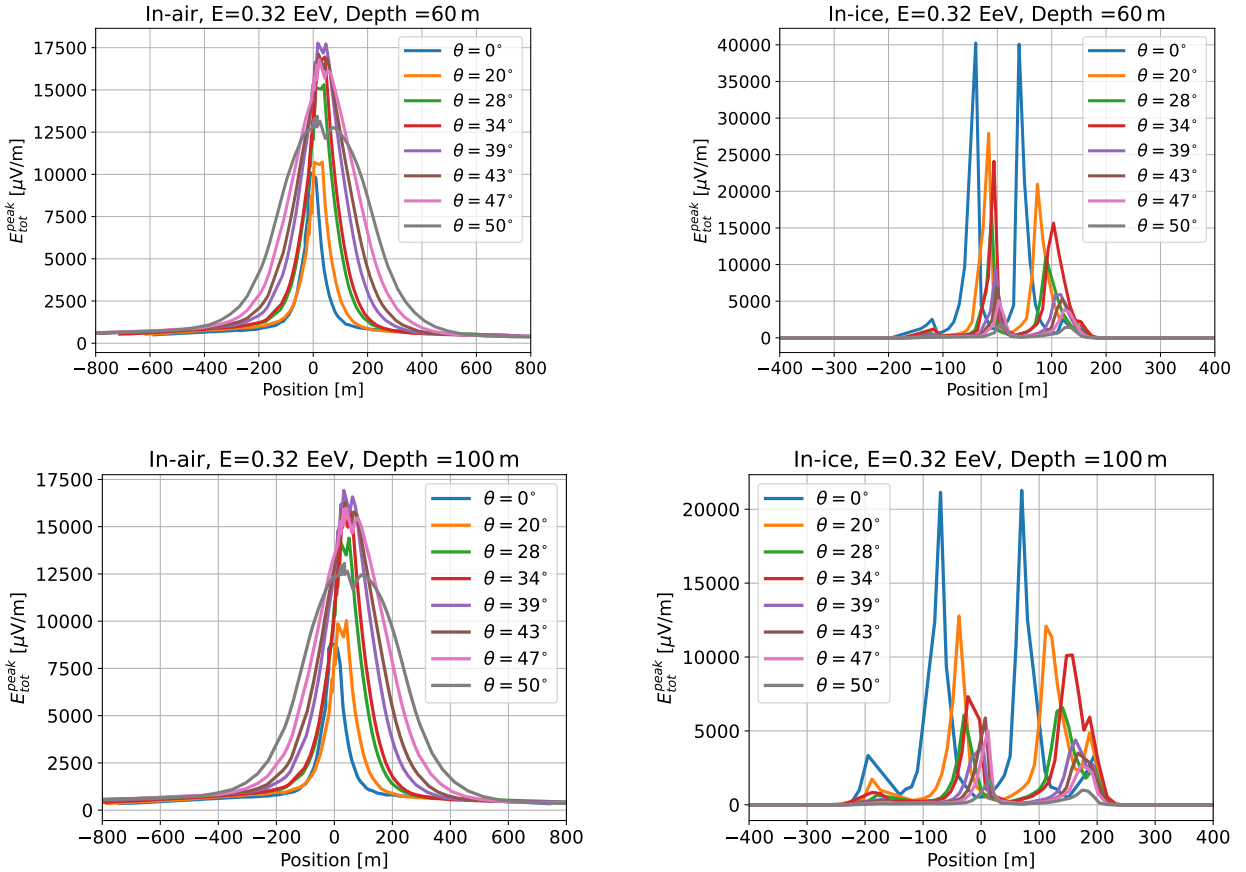


Figure 6: Lateral distribution functions of the peak amplitude of the electric-field norm along the South-North axis, observed at a depth of 60 meters (top) and 100 meters (bottom), for the in-air (left) and in-ice (right) emissions. Simulated showers with primary energy  $E = 10^{17.5}$  eV were used. Each colored line corresponds to a different zenith angle.

By definition, the radiation energy is a calorimetric observable which quantifies the amount of energy which is radiated in terms of radio emission. Its dependency with the shower parameters can therefore be directly linked to the shower physics. In the following we evaluate and compare the radiation energy of the in-air and in-ice components of cosmic ray radio emission.

### 3.1. Consistency checks

The radiation energy is sensitive to the grid of antennas used to evaluate the radio signal and can be biased if the antenna grid is too sparse, which would deteriorate the interpolation of the radio signal, or if the grid is not large enough, in which case part of the radio footprint could be missing. Since we simulated a 3D grid of antennas a simple consistency check consists in evaluating the radiation energy using different layers of antennas independently. As the radiation energy

is conserved through propagation of the emission, for a single shower the radiation energy should be roughly the same independently of the layer used for its computation. In Fig. 7, we show the square root of the ratio of the radiation energy between showers with primary energy  $E = 10^{17.5}$  eV and  $E = 10^{17}$  eV, for different zenith angles. The left-hand panel corresponds to the in-air component while the right-hand panel is for the in-ice component. We note that for the in-ice emission we only included antenna layers at 60 and 100 meters since these are the most relevant ones to characterize the emission. We can observe that for a fixed zenith angle, the radiation energy is constant across all depths for both the in-air and the in-ice emission. Only a small deviation is observed for the in-ice component at a zenith angle of  $\theta = 43^\circ$ , but the variation still remains small. This implies that our simulation library can safely be used to characterize the radiation energy of the radio emission.

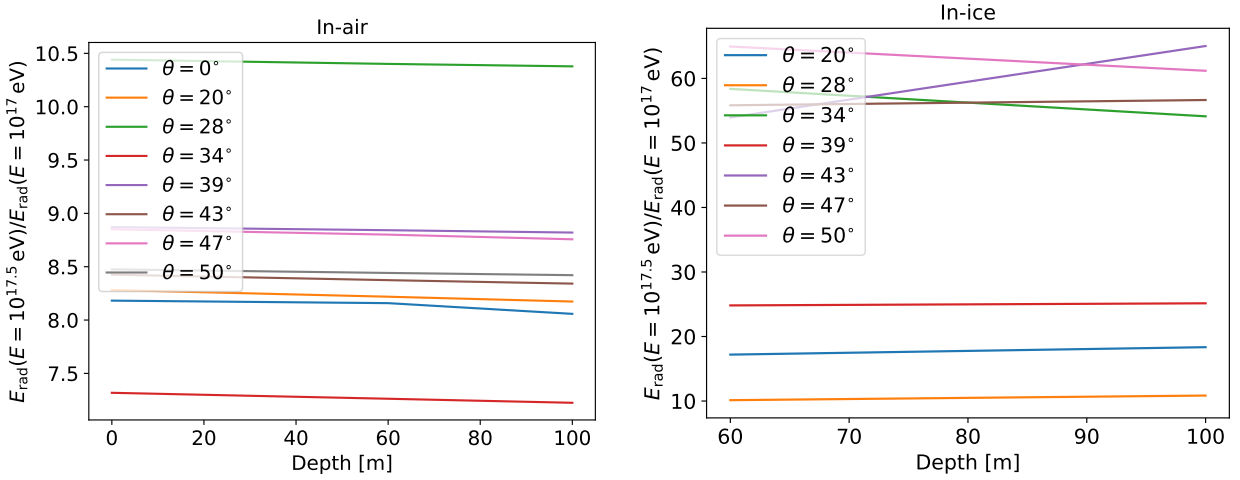


Figure 7: Radiation energy ratio for the in-air (left) and in-ice (right) emissions, between showers with primary energy  $E = 10^{17.5}$  eV and  $E = 10^{17}$  eV, for different zenith angles (colors), as a function of the antenna depth.

### 3.2. Energy scaling

From Fig. 7, we can also study the energy scaling of the radio emission. An increase in the primary energy leads, to first order, to a proportional increase in the number of particles at the in-air shower maximum [30], such that  $N_{\text{part}} \propto E_{\text{primary}}$ . For coherent radio emission, the radiation energy then scales with the square of the number of emitters,  $E_{\text{rad}}^{\text{air}} \propto N_{\text{part}}^2$ , implying  $\sqrt{E_{\text{rad}}^{\text{air}}} \propto E_{\text{primary}}$ . Since the radiation energy is defined as the time integral of the squared electric field, the electric-field amplitude must therefore scale linearly with the primary energy,  $\mathcal{E} \propto E_{\text{primary}}$ .

These scaling relations can be directly confirmed in Fig. 7. The ratio of the two primary energies considered is  $10^{17.5}/10^{17} = \sqrt{10}$ , which implies a factor of  $\sim 10$  in radiation energy. This is indeed approximately what is observed for the in-air component in Fig. 7. The fact that the values are on average slightly below 10 can be attributed to the fact that in practice the radiation energy rather scales with the electromagnetic component of the shower than with the total number of particles. On the other hand, the in-ice emission shows ratios well above 10 for some showers, which indicates that for this component,  $\sqrt{E_{\text{ice}}^{\text{rad}}}$  grows faster than linearly with the primary energy. This trend is further evidenced in Fig. 8, which shows the square root of the in-air and in-ice radiation energies as a function of the primary particle energy and the comparison to a linear scaling. Each data point on the figure corresponds to an average over the 8 zenith angles of our library while the error bars repre-

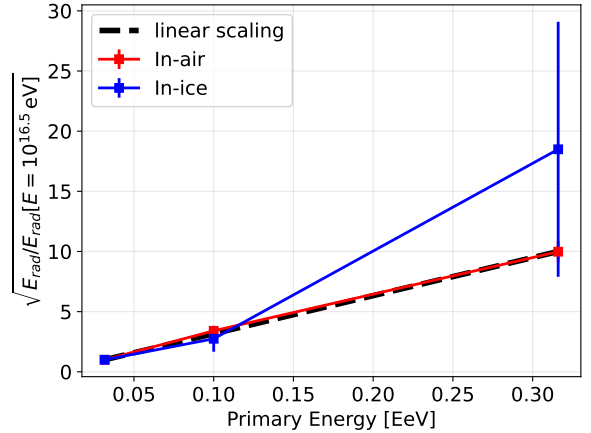


Figure 8: Square root of the in-air (red) and in-ice radiation energies, as a function of the primary particle energy and normalized by the value at  $10^{16.5}$  eV. Each data point corresponds to average over the 8 zenith angles of our library, while the error bars show the standard deviations of the distributions.

sent the standard deviations of the distributions. Before averaging, the radiation energy at each zenith was normalized to its value at  $10^{16.5}$  eV, so as to remove any dependence on the shower zenith angle. We observe that the in-air emission indeed follows a linear scaling while a super-linear scaling is observed for the in-ice component, particularly at the highest energies. The large error bars at high energy also indicate large variations of the in-ice energy scaling depending on the shower zenith angle.

To better constrain the energy scaling of the in-ice emission, we can decompose the problem into two

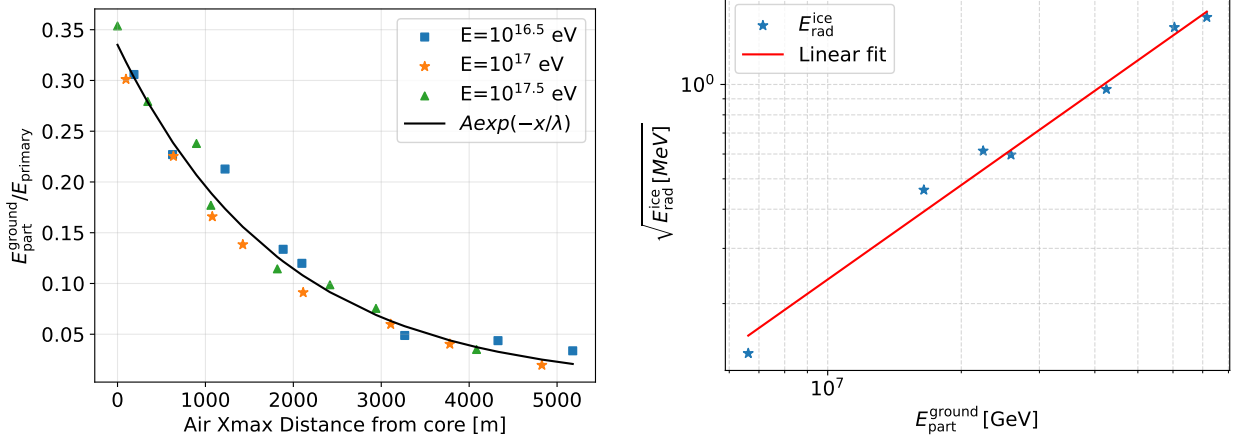


Figure 9: (Left) Total ground particle energy as a function of the distance from the in-air shower maximum  $X_{\text{max}}$ . The color and marker style codes for the various primary energies. The results are fitted with an exponential decay law (black line). (Right) Square root of the in-ice radiation energy as a function of the ground particle energy for simulated showers with primary energy  $E = 10^{17.5}$  eV. Each data point corresponds to a shower with different zenith angle. The results are fitted with a linear model.

steps. (1) We first evaluate the total particle energy at the ice surface,  $E_{\text{part}}^{\text{ground}}$ , and its dependence on the shower parameters. (2) We then relate  $E_{\text{part}}^{\text{ground}}$  to the in-ice radiation energy  $E_{\text{rad}}^{\text{ice}}$ . Indeed, following the same reasoning as for the in-air emission, the in-ice radiation energy should scale with the number of particles at the ice surface,  $E_{\text{rad}}^{\text{ice}} \propto (E_{\text{part}}^{\text{ground}})^2$ , rather than directly with the primary particle energy. The particle energy at the ice surface is expected to depend both on the shower primary particle energy and on the geometrical distance between the in-air  $X_{\text{max}}$  and the ice surface, since shower particles will lose their energy as they propagate in the atmosphere. We remove the first dependency by normalizing  $E_{\text{rad}}^{\text{ice}}$  to the primary energy, while we show the remaining dependency with the distance to  $X_{\text{max}}$ , obtained from FAERIE simulations, in left-hand panel of Fig. 9. We can observe that the normalized particle energy at the ice surface is in good agreement with an exponential decay following

$$\frac{E_{\text{rad}}^{\text{ice}}}{E_{\text{primary}}} = A \exp\left(-\frac{x}{\lambda}\right), \quad (4)$$

with  $A$  a proportionality factor and  $\lambda \sim 1800$  m the characteristic attenuation length of the particle cascades. The distance  $D_{\text{xmax}}$  of the shower core to the in-air  $X_{\text{max}}$ , itself depends only on the Earth's atmosphere and on the primary particle characteristics. Indeed, the primary particle mass composition and energy will determine its  $X_{\text{max}}$  [31] grammage, light energetic primaries usually penetrate deeper in the atmosphere than heavier/less energetic ones. Then given  $X_{\text{max}}$ , an atmospheric density model and the shower zenith angle, one can derive the  $X_{\text{max}}$  position and its distance to the Earth's surface.

In the right-hand panel of Fig. 9 we now show the square root of the in-ice radiation energy as a function of the total ground particle energy. Each data point corresponds to a given simulation at  $10^{17.5}$  eV, but with different zenith angle each, resulting in different values of  $E_{\text{part}}^{\text{ground}}$ . The in-ice radiation energy exhibits a clear linear dependence on the energy carried by the shower particles reaching the ice surface. A linear fit following

$$\sqrt{E_{\text{rad}}^{\text{ice}}} = a (E_{\text{part}}^{\text{ground}})^b, \quad (5)$$

yields a slope of  $b = 0.945 \pm 0.06$  and a coefficient of determination  $R^2 = 0.99$ , which confirms the expected scaling of the in-ice radiation energy with the ground particle energy.

The dependencies of the in-air and in-ice radiation energy evidenced in Fig. 8 and Fig. 9 are crucial. They allow FAERIE showers simulated at a limited set of energies to be rescaled to other energies, thereby providing large datasets while drastically reducing the computation time. Furthermore, these results should also be valuable for energy reconstruction of the primary particle.

### 3.3. Scaling with the zenith angle

We also studied the dependency of the in-air and in-ice radiation energies with the shower zenith angle. In

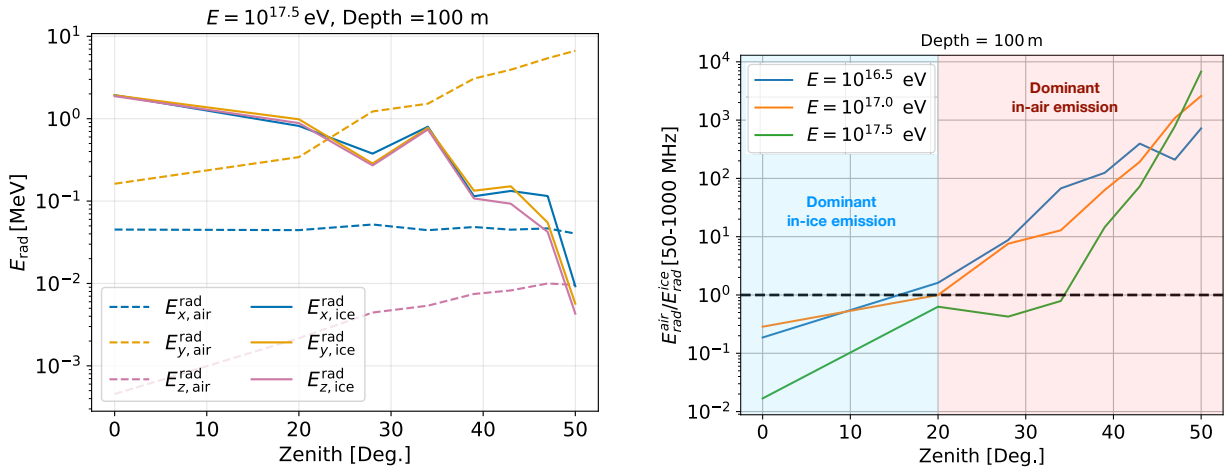


Figure 10: (Left) In-air (dashed line) and in-ice (solid lines) radiation energy associated with each channel of the electric field, as a function of the shower zenith angle. The results correspond to simulations with primary energy  $E = 10^{17.5}$  eV and the antenna layer at depth of 100 m was used to evaluate the radiation energy. (Right) Ratio between the in-air and in-ice radiation energies, as a function of the shower zenith angle, for three primary particle energies (colored lines). The black dashed line indicates the limit where the ratio is equal to 1.

the left-hand panel of Fig. 10 we show the radiation energy associated to each channel of both the in-air and in-ice emissions, as a function of the shower zenith angle, for simulations with primary energy  $E = 10^{17.5}$  eV. We observe two opposite behaviors between the in-air and the in-ice component. For all channels, the in-air radiation energy increases with the increasing zenith angle, while the in-ice radiation energy decreases. The trend for the in-ice component is related to the fact that for inclined showers the in-air  $X_{\text{max}}$  to shower core distance is larger, which results in a lower ground particle energy and a lower radiation energy as discussed in Section 3.2. Because of this dependency, the radio emission from the in-ice component becomes barely detectable for showers with a zenith angle of  $50^\circ$  (except for the most energetic events) and even weaker for more inclined showers.

For the in-air component, an overall increase of the radiation energy is expected for two main reasons. First, inclined showers develop at higher altitudes (Fig. 4), where the lower air density enhances the transverse-current emission (discussion Section 2.6). Moreover, the geomagnetic emission scales with  $\sin \alpha$ , with  $\alpha$  the so-called geomagnetic angle between the shower and the local magnetic field directions. In Greenland's near-vertical magnetic field this angle grows with zenith, further enhancing the radiation energy. Additionally, channel-dependent effects are expected as the geomagnetic emission is linearly polarized along the  $-\mathbf{v} \times \mathbf{B}$  direction. This direction initially corresponds to the  $y$ -axis for a vertical shower, but gets projected into the  $x$

and  $z$  directions when the shower gets inclined, therefore enhancing the signal in these channels.

In the right-hand panel of Fig. 10, we show the ratio between the in-air and in-ice radiation energies as a function of the shower zenith angle for the three primary energies of our library. It is clear that vertical showers are dominated by the in-ice emission, whereas for more inclined showers  $\theta \gtrsim 20^\circ$  the in-air component becomes dominant. Increasing the primary energy shifts the air/ice ratio to slightly lower values, as the two contributions scale differently (Section 3.2), but the overall trend remains unchanged. We note that this behavior represents an average feature of the emission. At the scale of individual antennas, the in-air/in-ice ratio may differ depending on the antenna position, but the trend observed in Fig. 10 remains a strong indicator of which component dominates in a given region of the parameter space and of the typical radio signatures (in-air or in-ice like) that should be targeted when reconstructing events. For example, neutrino showers are expected to arrive at the detector with rather horizontal trajectories, with zenith angles  $\theta \gtrsim 40^\circ$  [10], since they need to travel long enough in the ice to cascade in the medium. This implies that in the range of zenith angle where neutrinos are expected, the typical cosmic ray signals should be in-air like, i.e., dominated by the geomagnetic emission, hence with quite distinctive features than neutrino signals, which would be valuable for cosmic ray/neutrino discrimination.

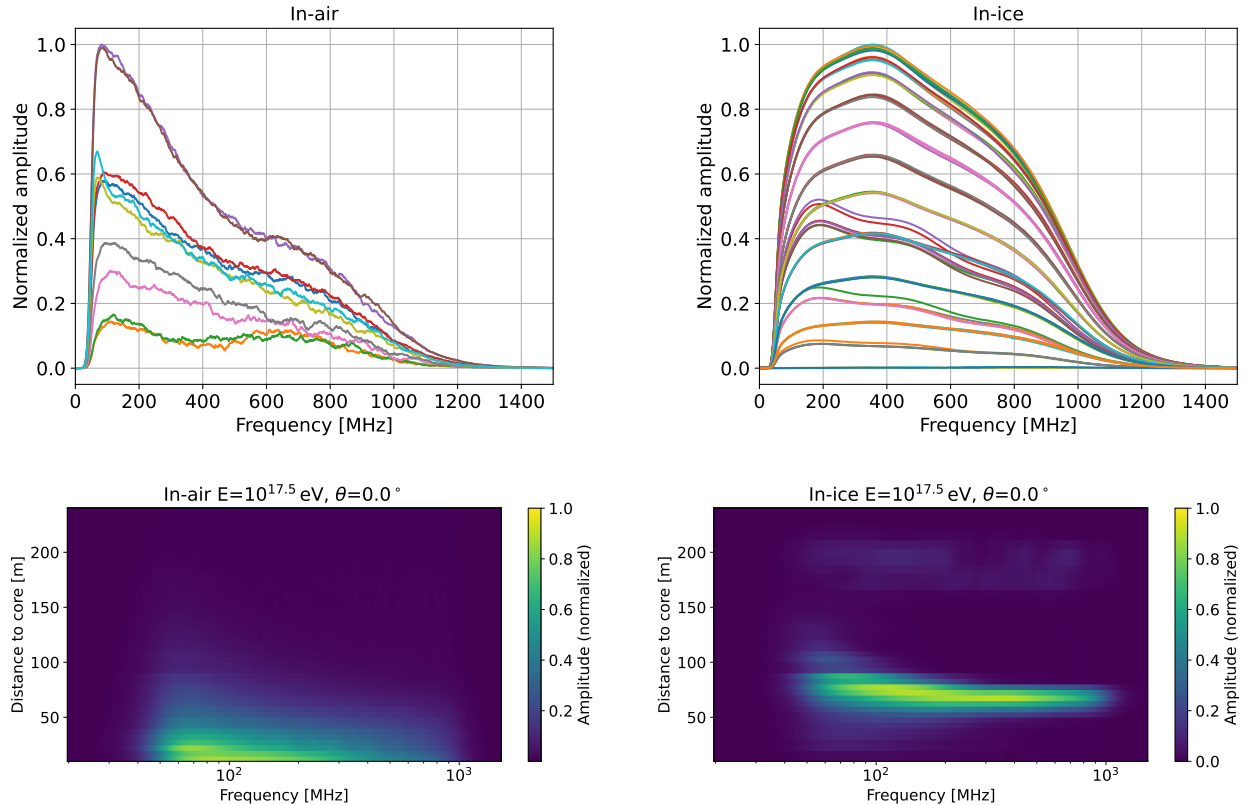


Figure 11: (Top) Frequency-domain amplitude spectra of several antennas for the in-air (left) and in-ice (right) emissions, observed at a depth of 100 meters, for a vertical proton shower with primary energy  $E = 10^{17.5} \text{ eV}$ . Antennas were placed at various radial distances (colors) near the Cherenkov cone of each emission. (Bottom) 2D heat maps of the in-air and in-ice frequency-domain amplitude spectra, for the same vertical proton shower. The color codes for the amplitude of each frequency, while the y-axis indicates the distance of the antennas from the shower core.

#### 4. Radio signal observables

Once we know which emission component of cosmic ray emission should be dominant, we can evaluate the characteristic signatures of each emission, that could be target to identify cosmic rays or discriminate them from neutrino primaries when analyzing experimental data.

##### 4.1. Frequency signatures

In-ice detectors such as ARA and RNO-G operate over a broad frequency range, typically from  $\sim 80$  to  $700$  MHz. This raises the possibility of using the frequency content of the radio signal to identify cosmic-ray signatures. The in-air and in-ice emissions from cosmic-ray showers are expected to exhibit distinctive frequency features: the air cascade has a characteristic size of hundreds of meters and therefore remains coherent only at relatively low frequencies, whereas the in-ice cascade develops over a few centimeters and can

produce coherent emission up to much higher frequencies.

In Fig. 11, we show frequency signatures of the in-air (left-hand panel) and in-ice (right-hand panel) emissions from FAERIE simulations, for a vertical proton shower with an energy  $E = 10^{17.5} \text{ eV}$ , observed at a depth of 100 meters. The top panels show the frequency-domain amplitude spectra of a few antennas located around the Cherenkov ring of each emission. The plot highlights that the in-air emission has a rather sharp amplitude spectrum, that peaks at low-frequency below 100 MHz. On the other hand, the in-ice emission shows a broad amplitude spectrum which peaks at much higher frequencies around  $\sim 400$  MHz. These features could already enable cosmic-ray identification or emission-mechanism discrimination at the single-antenna level, using for example the ratio between the high to low frequency power.

The bottom panels of Fig. 11 show 2D heatmaps of the amplitude spectra as a function of the antenna dis-

tance from the shower core. These plots reveal that the in-air emission (left-hand panel) peaks at low frequencies and at small core distances, whereas for the in-ice emission (right-hand panel) the highest amplitudes occur at much higher frequencies and at larger distances, around 70 meters away from the core. The figure also illustrates the strong spatial variability of the in-ice signal: the emission is sharply confined around the Cherenkov cone, and shifts to lower frequencies both before and beyond the cone. This indicates that in the case where several antennas are triggered, the spatial variation of the frequency content could yield relevant information to identify cosmic rays. The map also exhibits broadband, low-amplitude frequency content around radial distances of about 200 m. This corresponds to the location of the double ring in the same simulation (see Fig. 16). In the time domain, this feature appears as an interference pattern with alternating peaks and dips. Its origin will be investigated further. Finally, we note that though the results are shown for only one shower, similar behavior is observed for showers with different primary energy and zenith angles.

#### 4.2. *Polarization signatures*

Using our simulation library, we also investigated the polarization of the radio signal of each emission. Detectors like ARA and RNO-G typically combine Hpol antennas, that measure the horizontal polarization of the radio signal, with Vpol antennas, that measure the vertical polarization of the emission [34]. The signal in the Vpols can be estimated using the  $z$ -channel of the electric field  $E^{V\text{pol}} = E_z$ , while the signal in the Hpols can be estimated using the quadratic sum of the signal in the  $x$  and  $y$  channels  $E^{\text{Hpol}} = \sqrt{E_x^2 + E_y^2}$ . Using these definitions, we can then investigate the polarization of the radio signal using the Hpol/Vpol ratio.

In Fig. 13, we show the distributions of the Hpol/Vpol peak amplitude ratio at the antenna level, at a depth of 100 m, for simulations with a primary energy of  $E = 10^{17.5} \text{ eV}$ , covering all zenith angles in our library. The in-air distribution contains more antennas than the in-ice one, as the in-air footprint is larger and therefore a greater number of antennas have a well-defined Hpol/Vpol ratio. The figure evidences that the in-air emission shows stronger Hpol signals and hence much higher Hpol/Vpol ratios than the in-ice component. This is expected, as the geomagnetic emission, which is the dominant component for the in-air mechanism, mainly projects in the horizontal plane, as shown in the left-hand panel of Fig. 10. Both in-air and in-ice distribu-

tions can clearly be resolved, implying that already at the antenna level, the polarization of the radio signal could help discriminate between the in-air and in-ice emissions from cosmic ray showers. Furthermore, since the neutrino emission is typically Askaryan-like, this also implies that the polarization could help discriminate between the in-air cosmic ray emission and the in-ice Askaryan emission from neutrino showers. We note, however, that in practice we will not directly measure the radio signal polarization, but rather the signal voltage which corresponds to the projection of the electric field along the antenna effective length. This will of course deteriorate the polarization. Still, some of the features observed at the electric field should remain and could still be visible in the voltage.

We can also evaluate the total radiation energy measured by the Hpol and Vpol antennas by substituting  $E^{\text{Hpol/Vpol}}$  in Eqs. (2) and (3). In Fig. 12, we show the ratio of Hpol and Vpol radiation energies  $E_{\text{rad}}^{\text{Hpol}}/E_{\text{rad}}^{\text{Vpol}}$ , as a function of the shower zenith angle, for both the in-air (left-hand panel) and in-ice emissions (right-hand panel). The results are averaged over the three primary energies of our library, the dots indicate the average results while the error bars show the standard deviations of the distributions. As the radiation energy corresponds to an average result over many antennas we can see that the difference in the Hpol/Vpol ratio becomes even more relevant on these plots with more than 2 orders of magnitude difference, independently of the shower zenith angle. For the in-air emission, the vertical case stands out, as it corresponds to a case where the in-air  $X_{\text{max}}$  can be below the ice for the most energetic showers (Fig. 4), which also explains the large error bars, when averaging over several energies. For more inclined showers we can observe a continuous increase of the Hpol/Vpol ratio with increasing zenith angle. This trend arises because the geomagnetic emission strengthens for inclined showers—due to both the lower density at  $X_{\text{max}}$  and the larger geomagnetic angle (see Section 3.3)—while the Askaryan contribution weakens as the reduced air density at  $X_{\text{max}}$  suppresses the charge-excess emission [32, 35]. For the in-ice emission, the radial polarization impose similar amplitudes in each channel as shown in Fig. 10. This yields a roughly constant ratio around 2, since the radiation energy scales with the squared electric field. For more inclined showers, a slight increase is observed, which we associate to ray bending effects that become more prominent for more horizontal showers and that will shift the polarization. These results highlight that in the case where an event is seen by several antennas, averaging the signals over the antennas should make the polarization signa-

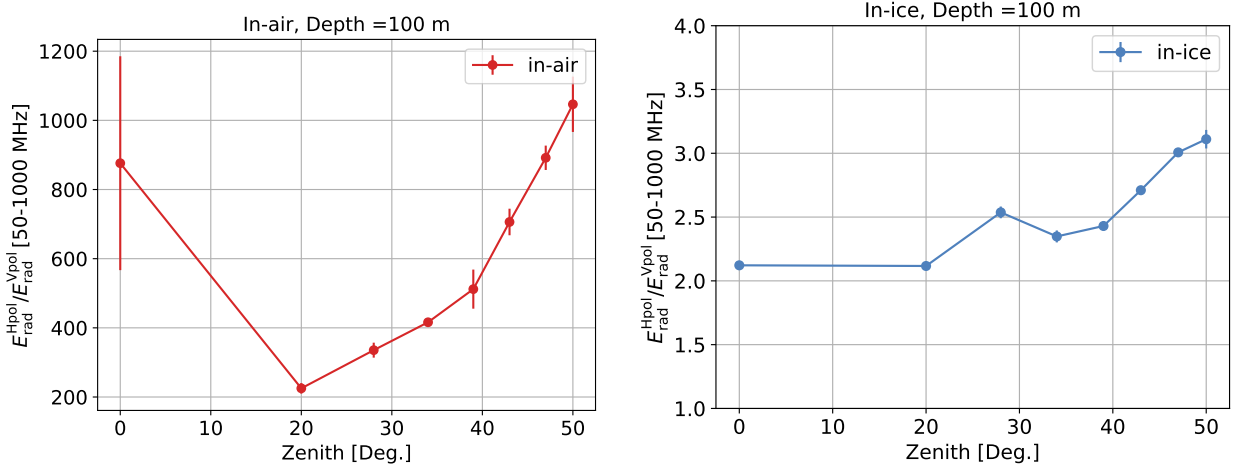


Figure 12: Ratio of the radiation energy measured in the Hpol and Vpol antennas for the in-air (left) and in-ice (right) components, as a function of the shower zenith angle. The results are averaged over the three primary energies of our library, the dots correspond to the mean and the error bars to the RMS of the distribution.

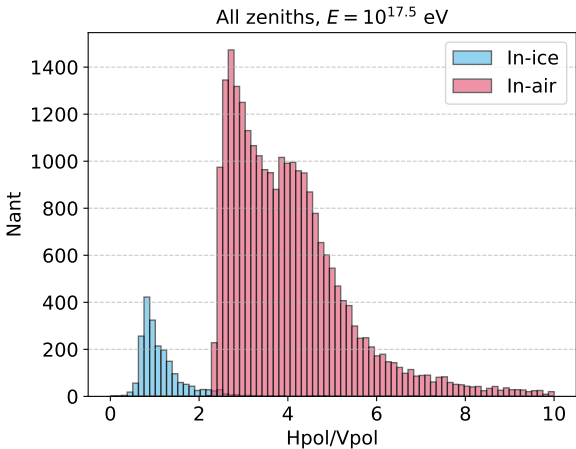


Figure 13: Distribution of the Hpol/Vpol ratio of the in-air (red) and in-ice (blue) components, observed at a depth of 100 meters, from FAERIE simulations for showers with primary energy  $E = 10^{17.5}$  eV, and zenith angle between  $0^\circ$  and  $50^\circ$ . The Hpol signal is defined as  $E^{\text{Hpol}} = \sqrt{E_x^2 + E_y^2}$ , the Vpol signal is defined as  $E^{\text{Vpol}} = E_z$ .

ture even more significant.

#### 4.3. Double pulses

In the case where both emissions overlap, the in-air and in-ice signals from cosmic ray showers can sometimes reach the same antenna and give rise to a typical double pulse signal. We illustrate such a signal in the left-hand panel of Fig. 14. The in-air pulse usually always arrives before the in-ice one, since to first

order, the in-air emission propagates roughly along a straight line, while the in-ice cascade propagates along the shower axis and then the signal is emitted at the in-ice Cherenkov angle  $\theta_c^{\text{ice}} \sim 55^\circ$ . The amplitude ratio and delay between the two pulses depend on many parameters and can be linked to shower properties (primary energy, zenith angle) and observer position.

Using FAERIE simulations, we can investigate the occurrence of double pulse events. Setting the background level at  $\sigma = 20 \mu\text{V/m}$ , we assume that a double pulse is observed at a given antenna if (1) there is at least one pulse with a peak amplitude in the norm of the electric field above  $5\sigma$ , (2) there is a second pulse with a peak amplitude above  $3\sigma$  and (3) the two pulses are separated by at least 50 ns. These conditions ensure that the antenna “triggers”, that second, low-amplitude pulse can be distinguished from the noise, and that the in-air and in-ice pulses can be resolved even after additional timing uncertainties from the detector response. In Fig. 15 we show maps of the double pulse spatial distribution at a depth of 100 meters, for a vertical shower ( $\theta = 0^\circ$ ) and an inclined shower ( $\theta = 50^\circ$ ) with primary energy  $E = 10^{17.5}$  eV. By comparing with the fluence footprints in Fig. 16, we see that the double-pulse distributions generally follow the in-ice footprints. For the vertical shower, this is mainly due to the strong spatial variability of the in-ice emission, whose amplitude peaks at the Cherenkov cone and drops rapidly away from it. For the inclined shower, the in-air footprint encompasses the in-ice one, whose amplitude is subdominant. A double pulse therefore appears only when the in-ice emission exceeds the thresholds defined above.

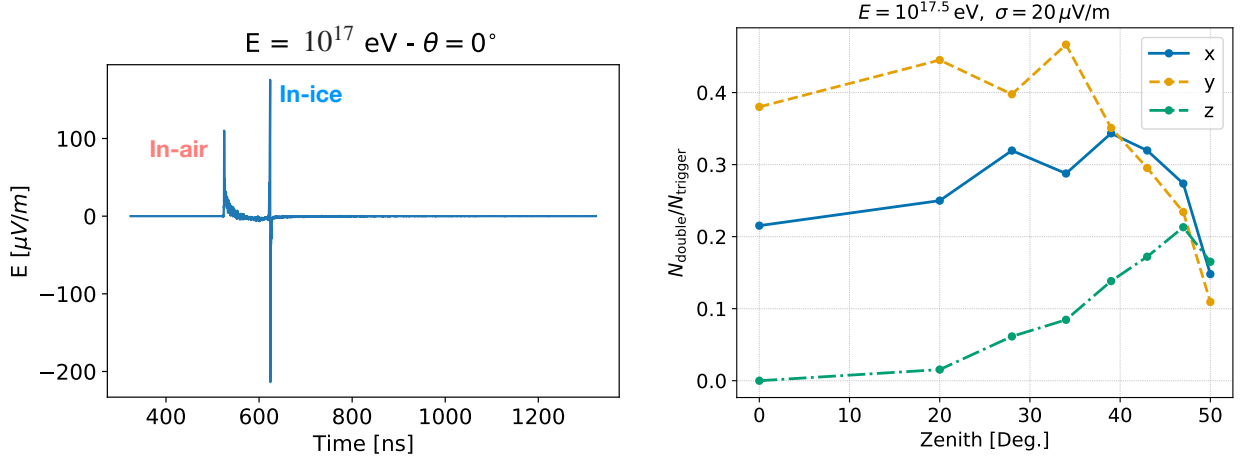


Figure 14: (Left) Typical double pulse signal measured at a given antenna at a depth of 100 meters, from FAERIE simulations. (Right) Double pulse rate per channel, observed at a depth of 100 meters, as a function of the shower zenith angle, for primary particles with energy  $E = 10^{17.5}$  eV. The double pulse rate is given by the number of antennas seeing a double-pulse events divided by the number of triggered antennas.

Increasing the trigger thresholds or decreasing the primary particle energy yields globally similar results, with a reduced number of double pulse events. Typically, at lower energy, the map for the vertical exhibits a deficit of double pulses where the geomagnetic and charge-excess mechanisms interfere destructively, due to the in-air emission becoming subdominant.

Eventually, for each simulation we evaluated the number of antennas seeing a double pulse  $N_{\text{double}}$ , using the criteria defined above. We note that we divided the threshold conditions by a factor  $\sqrt{3}$  to account for the fact that we work here with the individual channel level and not with the electric field norm. Similarly, for each channel we evaluated the total number of triggered antennas, i.e., the number of antennas with a peak electric field amplitude  $5\sigma/\sqrt{3}$ . The double pulse rate is then estimated from the ratio of these two quantities  $r_{\text{double}}$ .

Finally, we investigate the rate of double-pulse events observed in each channel. For each simulation, we estimate the number of antennas exhibiting a double pulse,  $N_{\text{double}}$ , using the criteria defined above. Since this analysis is performed at the individual channel level rather than on the electric-field norm, the threshold conditions are divided by a factor  $\sqrt{3}$ . Likewise, for each channel we determine the total number of triggered antennas, defined as those with a peak electric-field amplitude exceeding  $5\sigma/\sqrt{3}$ . The double pulse rate is then estimated from the ratio of these two quantities  $r_{\text{double}}$ . In the right-hand panel of Fig. 14, we present the double-pulse rate per channel at a depth of 100 m as a function of the shower zenith angle for simulations with a primary energy of  $E = 10^{17.5}$  eV. A significant fraction

of triggered events exhibit a double pulse, reaching up to  $\sim 40\%$  in the  $y$ -channel. The dependence on zenith angle can be understood as follows. For nearly vertical showers, the in-air component is subdominant (see Fig. 10). As the shower inclination increases, the in-air radiation energy grows in all channels and its spatial extent broadens, leading to a corresponding increase in the double-pulse rate. For the most inclined showers, however, the in-ice emission becomes subdominant and too weak to produce a clearly distinguishable pulse, causing the double-pulse rate to decrease. Consequently, the highest rate of double pulse events is observed at the intermediate zenith angle of  $\theta \sim 34^\circ$ . The figure also shows that double pulses are far more likely to be observed in the Hpol antennas (high rate in the  $x$  and  $y$  channels) than in the Vpol antennas  $z$ . Hence, comparing the rate of double pulses in these two types antennas could help identify cosmic ray signals or reconstruct their zenith angle. Similar results are observed when using the antenna layer at a depth of 60 meters. Decreasing the primary energy or increasing the trigger thresholds will mainly decrease the observed rate while roughly preserving the global trend. For example, the maximum rate of the double pulse events falls to  $\sim 20\%$  for showers with primary energy  $E = 10^{16.5}$  eV, and no double pulse is observed in the  $z$ -channel for showers with primary energies below or equal to  $E = 10^{17}$  eV.

## 5. Discussion

Radio emission from cosmic ray particle showers exhibit numerous features that would be useful for their iden-

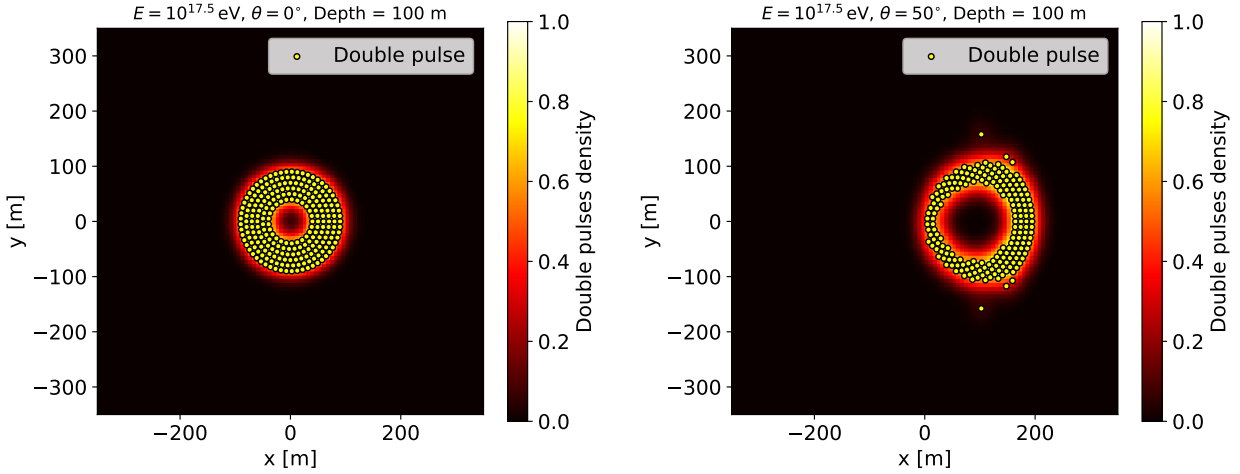


Figure 15: Heatmap of double pulse distribution, for a vertical  $\theta = 0^\circ$  and inclined  $\theta = 50^\circ$  shower, with primary energy  $E = 10^{17.5}$  eV, observed at a depth of 100 meters. Each yellow dot corresponds to an antenna seeing a double pulse, the color scales with the number of double pulses.

tification and to guide future analysis. Furthermore, the differences between the in-air and in-ice components will be valuable to discriminate between both, but also to discriminate the in-air cosmic ray emission from neutrinos, since neutrinos signatures should typically be Askaryan-like. We note that these results were obtained at the electric field level, using raw outputs of FAERIE simulations. Hence, to evaluate the true background rejection efficiency and discrimination power that could be reached, one would need to incorporate the detector response chain and the noise background environment. Indeed, in experimental conditions, signatures such as the radio signal polarization, frequency and amplitude distributions will be modified by the detector gain, bandwidth, effective length... Still, some of these features should remain and for example a recent study on the first observation of in-ice cosmic ray signals, performed by ARA typically used some of the radio signal observables mentioned in this study [14] (polarization and frequency spectrum).

Identifying cosmic rays with in-ice radio detectors will be challenging, and towards that goal, experiments could rely on the arrival direction of the signals. Indeed, cosmic rays interact first in the atmosphere hence detectors like RNO-G use surface antennas to veto cosmic rays and discriminate them from neutrino primaries. Reconstructing the true arrival direction of the radio emission should also be valuable, as we have shown that in-air and in-ice cosmic ray signatures both have a strong dependence on the shower zenith angle. Particularly, the fact that the in-air component dominate for inclined showers (Section 10) should drastically ease the

discrimination with neutrino emission. The rapid variation of the in-ice signal with the antenna depth mentioned in Section 2.6 also provides a valuable way to remove any far above surface background source. Double pulses will be the most qualitative detectable events, allowing us to observe characteristics of the in-air and in-ice emissions, at the single antenna level, after they went through the same detection chain. These events will represent of significant fraction of triggered events (Section 4.3) and their observation, with the first pulse matching the characteristics of the in-air emission and the second pulse matching of the in-ice emission would be a smoking gun of cosmic ray emission. Eventually, the scaling relations evidenced in Sections 3.2 and 3.3 could allow us to build huge datasets of simulations and to reconstruct cosmic rays using template matching methods.

## 6. Conclusion

Particle cascades induce by high energy cosmic rays will emit in-air and in-ice radio emission that could be detected with in-ice neutrino detectors such as ARA, RNO-G, RET and IceCube-Gen2 radio. Using FAERIE Monte-Carlo simulations, we investigated radio signatures of cosmic ray particle cascades, based on the signal amplitude, radiation energy, frequency, polarization, and timing. Our results show that the in-ice component from cosmic ray emission should be dominant for vertical showers, while the in-air component dominates for inclined showers, with zenith angle  $\theta \gtrsim 20^\circ$ . We further showed that the in-air and in-ice component have differ-

ent signatures: The emission from the in-air component peaks at low frequency (below 100 MHz), close to the shower core and has a dominant Hpol polarization. On the other hand, the emission from the in-ice component peaks at higher frequencies (around 400 MHz), further away from the shower core and shows a radial polarization. Eventually, we investigated the spatial distribution of double pulse events and estimated their rate to represent up to  $\sim 40\%$  of triggered events in the y-channel of the electric field. These results provide valuable guidelines to identify cosmic rays and discriminate them from neutrinos with future in-ice radio experiments.

#### *Acknowledgments*

S. Toscano and S. Chiche are supported by the Belgian Funds for Scientific Research (FRS-FNRS).

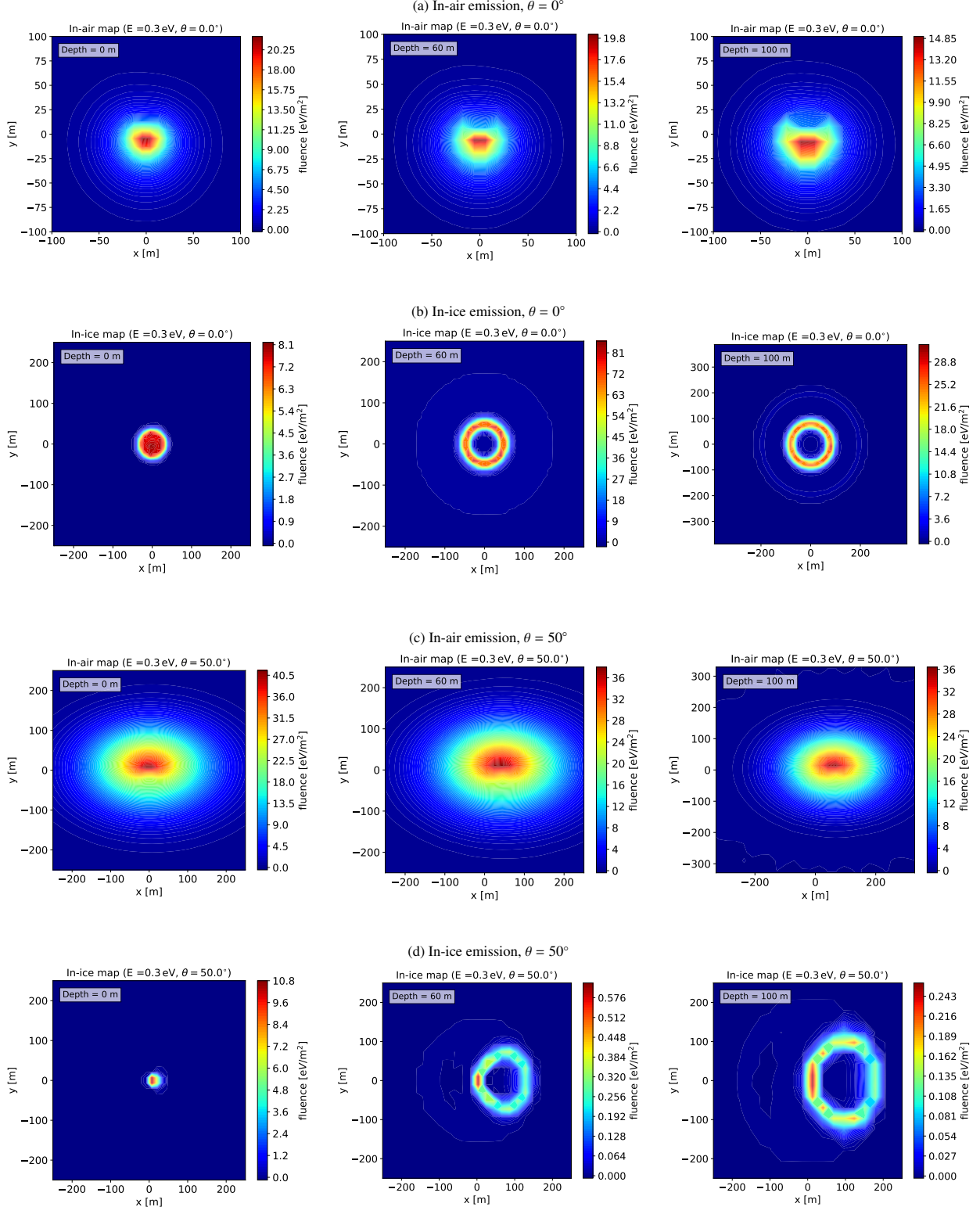


Figure 16: Interpolated electric-field maps of in-air and in-ice emission for proton showers at  $10^{17.5}$  eV, at zenith angles  $0^\circ$  and  $50^\circ$ , and for antenna depths of 0, 60 and 100 m. Each row corresponds to a different shower geometry, and each mini-caption summarizes the conditions.

## References

[1] M. Ackermann, et al., High-energy and ultra-high-energy neutrinos: A Snowmass white paper, *Journal of High Energy Astrophysics* 36 (2022) 55–110. [arXiv:2203.08096](https://arxiv.org/abs/2203.08096), doi:10.1016/j.jheap.2022.08.001.

[2] S. Aiello, et al., Observation of an ultra-high-energy cosmic neutrino with KM3NeT, *Nature* 638 (8050) (2025) 376–382, [Erratum: *Nature* 640, E3 (2025)]. doi:10.1038/s41586-024-08543-1.

[3] C. Guépin, K. Kotera, F. Oikonomou, High-energy neutrino transients and the future of multi-messenger astronomy, *Nature Reviews Physics* 4 (11) (2022) 697–712. [arXiv:2207.12205](https://arxiv.org/abs/2207.12205), doi:10.1038/s42254-022-00504-9.

[4] G. A. Askar'yan, Excess Negative Charge of an Electron-Photon Shower and its Coherent Radio Emission, *Zh. Eksp. Teor. Fiz.* 41 (1961) 616–618.

[5] J. Alvarez-Muñiz, A. Romero-Wolf, E. Zas, Practical and accurate calculations of Askaryan radiation, *Phys. Rev. D* 84 (10) (2011) 103003. [arXiv:1106.6283](https://arxiv.org/abs/1106.6283), doi:10.1103/PhysRevD.84.103003.

[6] A. Coleman, et al., In-ice Askaryan emission from air showers: Implications for radio neutrino detectors, *Astroparticle Physics* 172 (2025) 103136. [arXiv:2410.08615](https://arxiv.org/abs/2410.08615), doi:10.1016/j.astropartphys.2025.103136.

[7] M. Ackermann, et al., Optical properties of deep glacial ice at the South Pole, *Journal of Geophysical Research (Atmospheres)* 111 (D13) (2006) D13203. doi:10.1029/2005JD006687.

[8] S. Barwick, D. Besson, P. Gorham, D. Saltzberg, South Polar in situ radio-frequency ice attenuation, *J. Glaciol.* 51 (2005) 231–238. doi:10.3189/172756505781829467.

[9] ARA Collaboration, Performance of two Askaryan Radio Array stations and first results in the search for ultrahigh energy neutrinos, *Phys. Rev. D* 93 (8) (2016) 082003. [arXiv:1507.08991](https://arxiv.org/abs/1507.08991), doi:10.1103/PhysRevD.93.082003.

[10] J. A. Aguilar, et al., Design and sensitivity of the Radio Neutrino Observatory in Greenland (RNO-G), *Journal of Instrumentation* 16 (3) (2021) P03025. [arXiv:2010.12279](https://arxiv.org/abs/2010.12279), doi:10.1088/1748-0221/16/03/P03025.

[11] Radar Echo Telescope Collaboration, The Radar Echo Telescope for Cosmic Rays: Pathfinder experiment for a next-generation neutrino observatory, *Phys. Rev. D* 104 (10) (2021) 102006. [arXiv:2104.00459](https://arxiv.org/abs/2104.00459), doi:10.1103/PhysRevD.104.102006.

[12] M. G. Aartsen, et al., IceCube-Gen2: the window to the extreme Universe, *Journal of Physics G Nuclear Physics* 48 (6) (2021) 060501. [arXiv:2008.04323](https://arxiv.org/abs/2008.04323), doi:10.1088/1361-6471/abbd48.

[13] C. Glaser, Probing ultra-high-energy neutrinos with the IceCube-Gen2 in-ice radio array, *arXiv e-prints* (2025) arXiv:2507.07813 [arXiv:2507.07813](https://arxiv.org/abs/2507.07813), doi:10.48550/arXiv.2507.07813.

[14] ARA Collaboration, Observation of In-ice Askaryan Radiation from High-Energy Cosmic Rays, *arXiv e-prints* (2025) arXiv:2510.21104 [arXiv:2510.21104](https://arxiv.org/abs/2510.21104), doi:10.48550/arXiv.2510.21104.

[15] S. De Kockere, D. Van den Broeck, U. A. Latif, K. D. de Vries, N. van Eijndhoven, T. Huege, S. Buitink, Simulation of radio signals from cosmic-ray cascades in air and ice as observed by in-ice Askaryan radio detectors, *Phys. Rev. D* 110 (2) (2024) 023010. [arXiv:2403.15358](https://arxiv.org/abs/2403.15358), doi:10.1103/PhysRevD.110.023010.

[16] D. Heck, J. Knapp, J. N. Capdevielle, G. Schatz, T. Thouw, CORSIKA: a Monte Carlo code to simulate extensive air showers., 1998.

[17] J. Allison, et al., Recent developments in GEANT4, *Nuclear Instruments and Methods in Physics Research A* 835 (2016) 186–225. doi:10.1016/j.nima.2016.06.125.

[18] T. Huege, M. Ludwig, C. W. James, Simulating radio emission from air showers with CoREAS, in: R. Lahmann, T. Eberl, K. Graf, C. James, T. Huege, T. Karg, R. Nahnhauer (Eds.), 5th International Workshop on Acoustic and Radio EEV Neutrino Detection Activities: Arena 2012, Vol. 1535 of American Institute of Physics Conference Series, AIP, 2013, pp. 128–132. [arXiv:1301.2132](https://arxiv.org/abs/1301.2132), doi:10.1063/1.4807534.

[19] F. G. Schröder, Radio detection of cosmic-ray air showers and high-energy neutrinos, *Progress*

in Particle and Nuclear Physics 93 (2017) 1–68. [arXiv:1607.08781](https://arxiv.org/abs/1607.08781), doi:10.1016/j.ppnp.2016.12.002.

[20] T. Huege, Radio detection of cosmic ray air showers in the digital era, Physics Reports 620 (2016) 1–52. [arXiv:1601.07426](https://arxiv.org/abs/1601.07426), doi:10.1016/j.physrep.2016.02.001.

[21] O. Scholten, K. Werner, F. Rusydi, A macroscopic description of coherent geo-magnetic radiation from cosmic-ray air showers, Astroparticle Physics 29 (2) (2008) 94–103. [arXiv:0709.2872](https://arxiv.org/abs/0709.2872), doi:10.1016/j.astropartphys.2007.11.012.

[22] K. Werner, K. D. de Vries, O. Scholten, A realistic treatment of geomagnetic Cherenkov radiation from cosmic ray air showers, Astroparticle Physics 37 (2012) 5–16. [arXiv:1201.4471](https://arxiv.org/abs/1201.4471), doi:10.1016/j.astropartphys.2012.07.007.

[23] K. D. de Vries, O. Scholten, K. Werner, The air shower maximum probed by Cherenkov effects from radio emission, Astroparticle Physics 45 (2013) 23–27. [arXiv:1304.1321](https://arxiv.org/abs/1304.1321), doi:10.1016/j.astropartphys.2013.02.003.

[24] J. Alvarez-Muñiz, W. R. Carvalho, E. Zas, Monte Carlo simulations of radio pulses in atmospheric showers using ZHAireS, Astroparticle Physics 35 (6) (2012) 325–341. [arXiv:1107.1189](https://arxiv.org/abs/1107.1189), doi:10.1016/j.astropartphys.2011.10.005.

[25] C. W. James, H. Falcke, T. Huege, M. Ludwig, General description of electromagnetic radiation processes based on instantaneous charge acceleration in “endpoints”, Phys. Rev. E 84 (2011) 056602. doi:10.1103/PhysRevE.84.056602. URL <https://link.aps.org/doi/10.1103/PhysRevE.84.056602>

[26] S. Chiche, N. Moller, A. Bishop, S. de Kockere, K. D. de Vries, U. Latif, S. Toscano, Radio signatures of cosmic-ray showers with deep in-ice antennas, arXiv e-prints (2024) arXiv:2409.02185arXiv:2409.02185, doi:10.48550/arXiv.2409.02185.

[27] S. Chiche, K. D. de Vries, S. Toscano, Radio Signatures of Cosmic-Ray Particle Showers in Deep In-Ice Antennas, PoS ICRC2025 (2025) 221. doi:10.22323/1.501.0221.

[28] A. Aab, et al., Combined fit of spectrum and composition data as measured by the Pierre Auger Observatory, J. Cosmology Astropart. Phys.2017 (4) (2017) 038. [arXiv:1612.07155](https://arxiv.org/abs/1612.07155), doi:10.1088/1475-7516/2017/04/038.

[29] C. Deaconu, A. G. Vieregg, S. A. Wissel, J. Bowen, S. Chipman, A. Gupta, C. Miki, R. J. Nichol, D. Saltzberg, Measurements and modeling of near-surface radio propagation in glacial ice and implications for neutrino experiments, Phys. Rev. D98 (4) (2018) 043010. [arXiv:1805.12576](https://arxiv.org/abs/1805.12576), doi:10.1103/PhysRevD.98.043010.

[30] J. Matthews, A Heitler model of extensive air showers, Astroparticle Physics 22 (5-6) (2005) 387–397. doi:10.1016/j.astropartphys.2004.09.003.

[31] R. Engel, D. Heck, T. Pierog, Extensive air showers and hadronic interactions at high energy, Ann. Rev. Nucl. Part. Sci. 61 (2011) 467–489. doi:10.1146/annurev.nucl.012809.104544.

[32] C. Glaser, M. Erdmann, J. R. Hörandel, T. Huege, J. Schulz, Simulation of radiation energy release in air showers, J. Cosmology Astropart. Phys.2016 (9) (2016) 024. [arXiv:1606.01641](https://arxiv.org/abs/1606.01641), doi:10.1088/1475-7516/2016/09/024.

[33] The RNO-G collaboration, Radio emission from airplanes as observed with RNO-G, Journal of Instrumentation 20 (11) (2025) P11015. [arXiv:2506.17522](https://arxiv.org/abs/2506.17522), doi:10.1088/1748-0221/20/11/P11015.

[34] RNO-G Collaboration, Instrument design and performance of the first seven stations of RNO-G, Journal of Instrumentation 20 (4) (2025) P04015. [arXiv:2411.12922](https://arxiv.org/abs/2411.12922), doi:10.1088/1748-0221/20/04/P04015.

[35] S. Chiche, K. Kotera, O. Martineau-Huynh, M. Tueros, K. D. de Vries, Polarisation signatures in radio for inclined cosmic-ray induced air-shower identification, Astroparticle Physics 139 (2022) 102696. [arXiv:2202.06846](https://arxiv.org/abs/2202.06846), doi:10.1016/j.astropartphys.2022.102696.